Single-Molecule Devices: Materials, Structures and Characteristics

Biswanath Mukherjee and Asim K. Ray

Centre for Materials Research, Queen Mary, University of London, Mile End Road, London E1 4NS, United Kingdom

A. K. Sharma and Danhong Huang

Air Force Research Laboratory, Space Vehicles Directorate, 3550 Aberdeen Avenue SE, Kirtland Air Force Base, NM 87117, USA

(Dated: May 10, 2016)

This review article provides a brief survey of materials, structures and current state-of-the-art techniques used to measure the charge conduction characteristics of single molecules. Single molecules have been found to exhibit several unique functionalities including rectification, negative differential resistance and electrical bistable switching, all which are necessary building blocks for the development and configuration of molecular devices into circuits. Conjugated organic molecules have received considerable interest for their low fabrication cost, three dimensional stacking and mechanical flexibility. Furthermore, the ability of molecules to self-assemble into well-defined structures is imperative for the fabrication of molecular based circuits. The experimental current-voltage results are discussed using basic principles of carrier transport mechanisms.

PACS numbers: 87.15.hj

Contents

I. Introduction 1

II. Background 2

III. Charge Transport and Tunneling in Single Molecule Devices 2

IV. Single Electron Transistor Characteristics 3
- A. Coulomb Blockade Effects 3
- B. Ballistic Transport 5
- C. Surface-Plasmon Coupling 6

V. Effect of External Parameters 8
- A. Mechanical Force 8
- B. Environment Effect 8
- C. Local-Heating (Joule) Effects 8
- D. Energy Level Alignment of Molecule 9
- E. Mechanically Controllable Break Junction (MCBJ) 9

VI. Preparation of Self-Assembled Monolayers (SAM) 9

VII. Molecular Imaging Methods 11
- A. Scanning Probe Microscope (SPM) 11
- B. Scanning Tunneling Microscope (STM) 11
- C. Atomic Force Microscope (AFM) 11
- D. Conducting Atomic Force Microscope (C-AFM) 12

VIII. Nanopores 12

IX. Mercury (Hg) Drop Method 12

X. Summary 13

Acknowledgments 13

References 13

I. INTRODUCTION

The study of single molecule devices is of great interest to the scientific community at large. In the past two decades numerous advancements in manufacturing nanoscale materials with atomic precision have enabled the synthesis/fabrication of true molecular size devices. The ability to fabricate single molecule size devices has opened the door to a wide range of potential applications in diversified fields of modern quantum electronics (1; 2).

The charge conduction process in a single molecule is not merely a function of the intrinsic properties of a molecule, but it is coupled with the type of metal contacts that is made to that molecule. Therefore, the over-all charge transport mechanism is a complex function of the molecule, metal-molecule-metal contact bond type, affinities, work function differences, and the local environment. To explore a single molecules electronic functionality, a number of sophisticated tools have been developed in the recent years that can make repeatable and reliable contacts with single molecules, under a variety of metal-molecule-metal configurations.

In order to illustrate the impact of the electronic charge states in the nanoscale regime, lets for example consider a conventional planar metal-oxide-semiconductor (MOS) field effect transistor with a gate oxide thickness of $5\,nm$. If this transistors gate has both width and length of $100\,nm$, and we apply a $1\,V$ on the gate, about 300 electrons would reside in the channel. A fluctuation of only 30 electrons would give rise to voltage fluctuations of $0.1\,V$. Now if we extend this example, to the molecular regime, by considering a single molecule device that is only a few nanometers in length (smaller than the mean free path of an electronic charge) its corresponding electronic spectrum would be quantized to a few eV. Therefore, the key requirement towards developing single molecule electronic devices is greatly dependent on ones ability to precisely fabricate them with atomic scale precision and be able to measure the exact amount of charge fluctuations. Furthermore, in order to accurately model the mechanism of the charge transport process, the theoretical models need to include all sources of electric and magnetic

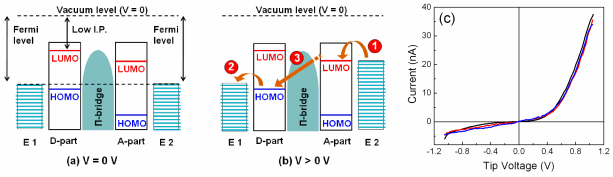

FIG. 1 (Color online) Energy band diagram of a D-π-A molecular junction. (a) under no bias condition and (b) under positive bias. Arrows in part (b) represent the electron transfer. (c) STM measurement of current-voltage characteristics (multiple scans) of a thin film of D-A supramolecule (D = CuPc, A = Rose Bengal).

fields that the molecule is subjected to, which may be part of a chemical or biological system (1). Additionally, the study of single molecule conductance enables one to extract information about the chemical and electronic states of a molecule. This information would be useful for further configuring the single molecule into for chemical or biosensor device applications (2; 3). This article provides a survey of the materials, structures and experimental techniques required to measure the current-voltage characteristics of a single molecule. The experimental carrier conduction results are then presented based on basic principles of carrier transport mechanisms.

II. BACKGROUND

Since Aviram and Ratner (4) predicted that theoretically individual molecules could function as electronic devices, tremendous research efforts have been put to investigate the electrical conductivity of molecules connected with metallic electrode contacts in the nanoscale regime (5–8). It was postulated by Aviram and Ratner that a molecule with D-σ-A structure (D = donor, σ =sigma bridge, A = Acceptor) confined between two metallic electrode contacts could act as an rectifier provided the donor moiety has low ionization potential (I.P.) and the acceptor moiety has an high electron affinity (E.A.) However, the first experimentally measured molecular rectifier was found to have D-σ-A structure (9) instead of a D-π-A configuration. The rectification properties can be easily explained in terms of the energy band diagram of Figure 1.

Figure 1(a) depicts the thermal equilibrium Fermi level of a molecular system with electrode contracts having energy levels E1 and E2 respectively on each side. In this thermal equilibrium ($V = 0\,V$) the large energy barrier between the molecule and metal contracts impedes electron transfer. However, under positive bias ($V > 0\,V$), the energy level of contact E2 can be raised to the acceptors Lowest Unoccupied Molecular Orbital (LUMO) level. In this biased state, an electron from E2 (Figure 1(b), step 1) can now easily occupy the LUMO level. Consequently, in order to conserve the charge neutrality of the system, another electron would be kicked-out the donors Highest Occupied Molecular Orbital (HOMO) level to the opposite polarity electrode E1 (step 2). This would yield a D^{+}-π-A^{-} configuration which is unstable. Therefore, the molecule would need to relax to the ground state by transferring an electron through the π bridge from acceptor LUMO to donor HOMO (step 3). In the opposite direction (reverse bias condition) the whole charge conduction process would be limited by the energy barrier configuration of the system, thus resulting in a diode like behavior. Figure 1(c) shows the Scanning Tunneling Microscope (STM) induced current-voltage (I-V) characteristics of a monolayer of a donor (D) and acceptor (A) molecular thin film having a thickness of $5 - 6\,nm$.

D-A supramolecule devices been fabricated on silicon (Si) substrates via layer-by-layer (LbL) electrostatic assembly of a monolayer of a donor, viz, Copper (II) phthalocyanine (CuPc), and a monolayer of an acceptor, viz, fluorine dye (Rose Bengal) in sequence (10). Because the LbL deposition relies on the surface charge reversal during the electrostatic adsorption of each layer, the deposition of one molecular layer or monolayer is also assured. Electron flow is favorable in one bias direction while it is limited in the reverse direction in both D-A and A-D assemblies. The rectification ratio (RR) obtained in the CuPc-Rose Bengal molecular assembly at a bias of 1V is about 7 and this result has been highly reproducible. The I-V characteristics of the Si-substrate with Pr/Ir Scanning Tunneling Microscope (STM) tip was found to be symmetrical, which eliminates the possibility of any Si-substrates parasitic effects influencing the rectification process. It is also noted that in case of A-D assembly, higher current is obtained in a direction opposite to the D-A assembly when the polarity of the electrodes is kept the same. The experimental results fully support a true molecular property of the supramolecule, intrinsic to the asymmetry of D-A or A-D assemblies.

Some other interesting properties that are exhibited by single molecules are reversible redox switching (11), molecular switching (12), negative differential resistance (NDR) (13), and single molecular electronic circuits (14). Also, the detection and manipulation of electronic spin in molecules have yielded many novel applications in the newly growing field, popularly known as molecular spintronics, where the magnetic state of the molecule can be translated into an electrical effect (15–17). There are many properties of single molecule devices that yet remain to be explored, such as what happens when relatively large voltage biases are applied to single molecules, capable of causing significant deformation to their molecular structure.

III. CHARGE TRANSPORT AND TUNNELING IN SINGLE MOLECULE DEVICES

As the size of a molecular junction becomes smaller than the mean free path of the electronic charged carrier, that is comparable to the de Broglie wavelength, the carrier transport process becomes ballistic and cannot be easily explained using Ohms law. Since a molecule has large charge addition energy and a quantized excitation spectrum, when a micro-scale electrode is contacted with this molecule, it will have a strong effect on the overall conductance process of this molecular nanoscale junction. The observation of Coulomb blockade at low temperature in most single molecules corresponds

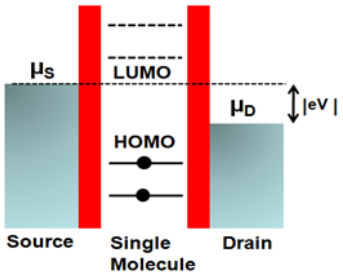

FIG. 2 (Color online) Energy level diagram of a single molecule device. Discrete lines denote the empty energy levels of the molecule, while the solid lines (below μ_S and μ_D) indicate levels occupied by an electron. μ_S and μ_D represent respectively the Fermi levels of source and drain.

to quantum excitations of the molecule and charge quantization. This also has the implications that the thermal energy of the electrons is significantly smaller than the Coulomb energy $e^2/2C$, where C is the total capacitance of the gate capacitor and the tunneling junctions. The junction conductance is much less than the quantum conductance $2e^2/h$, where, h is the Plancks constant. Thus, the quantum mechanical tunneling effect itself is considered to be weak enough to prevent the charge delocalization of the tunneling electrons. When the width of the molecular junction is less than the electrons mean free path, the resistance of the conducting channel, which is determined purely by quantum mechanical effects, is given in terms of Landauer resistance (18) $R = (h/2e^2)(1-T)/T$, where, T is the transmission coefficient. For 100% transmission for all-metal nanogap ($T = 1$), and the resistance is found to be quantized in units of $h/2e^2$. (19; 20)

The tunneling effect is observed when the insulating barrier is $\sim 1\,nm$ thick, i.e., a few atoms apart, and the transfer of charge follows the sequential tunneling process. Figure 2 shows the energy level diagram of a single molecule device with μ_S (source) and μ_D (drain) being the Fermi levels of the two electrodes and V the applied bias between the two electrodes satisfies the relation, i.e., $\mu_S - \mu_D = eV$. The discrete lines above μ_S and μ_D reflect the empty energy levels of the molecule, while the solid lines below μ_S and μ_D are occupied by one electron. The molecule-metal electrode contact is assumed to be opaque enough to serve as a tunnel barrier. For sequential tunneling to take place, there must be a state available between μ_S and μ_D, via which tunneling can occur. This results in large current flow through the junction (on-state). On the other hand, unavailability of electronic states between μ_S and μ_D, leads to blocking of charges with only a small current flow by direct tunneling process (off-state). The quantized electronic structure of a molecule causing on- and off-state, can be attributed to the charge addition energy and the electronic excitation spectrum.

IV. SINGLE ELECTRON TRANSISTOR CHARACTERISTICS

In order to explain the electron transport in a single molecule device let us use the Single Electron Transistor (SET) theory proposed initially by Kouwenhoven et al (21) and was described in detail by J. Park (22). Figure 3(a) shows the schematic representation of a SET device, where a quantum dot is coupled to all three electrodes capacitively. Although the tunnel barrier exists between the dot and all three electrodes, the electron tunneling is allowed only between the dot and source/drain electrodes. This also implies that an electron is either on the dot or one of the electrodes i.e. the number of electrodes on the dot is well defined.

If doped molecules on a chain are coupled strongly, electrons in this system can drift through a band-transport mechanism. However, the randomly-distributed impurities and lattice vibrations are still expected to introduce significant scattering on their way. If the length of a molecular chain becomes shorter than the mean-free-path of electrons, on the other hand, the electron motion can be ballistic with a quantized conductance.

A. Coulomb Blockade Effects

Figure 3(b) shows a family of I-V characteristics of a single electron transistor device fabricated from C_{140} molecule at different gate voltages (V_G). The results were obtained by J. Park (22). At low bias voltages, flow of electrons is limited/blocked (Coulomb Blockade) because of unavailability of sufficient energy of electrons to overcome the barrier energy in order to tunnel through the C_{140} molecule. An estimation of the source-drain voltage (V_{DS}) required to enable tunneling via the lowest-energy state of the molecule can be done from the two-dimensional plots of differential conductance (dI/dV) as a function of V_{DS} and V_G. However, an electron can tunnel through the barrier at very low source-drain bias, near $V_{DS} = 0$ for a specific value of gate voltage, $V_G = V_C$, where the charge states are degenerate (Coulomb Oscillation). This value of V_G is different for different devices/molecules because of differences in the local electrostatic environment. Therefore, we can make sure that as long as the measurements are performed sufficiently close to $V_G = V_C$, current flows only through a single molecule.

The electrostatic potential μ_{N+1} of the dot [refer to Figure 3(a)] is given by $\mu_{N+1} = U(N+1) - U(N)$, where $U(N)$ and $U(N+1)$ denote, respectively, the total energy for a dot having N and $N+1$ electrons. Therefore,

$$\mu_{N+1} = \sum_{i=1}^{N+1} E_i + \frac{(N+1)^2 e^2}{2C} - \sum_{i=1}^{N} E_i - \frac{N^2 e^2}{2C}$$

$$= E_{N+1} + \frac{(N+1/2)e^2}{C}\,, \qquad (1)$$

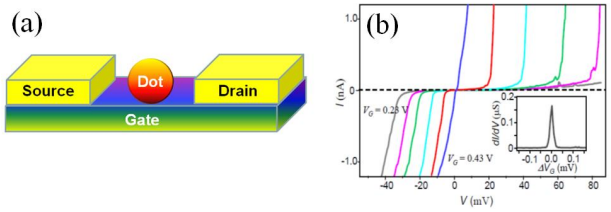

FIG. 3 (Color online) (a) Schematic of a single electron transistor device with allowed tunnel barrier between the small dot and source/drain electrodes. (b) I-V characteristics from a C_{140} single electron transistor. V_G increases in steps of $0.04\,V$ from gray ($0.23\,V$) to blue curve. Inset: the Coulomb oscillation curve from the same device. (Adapted from Ref. 23).

where E_i is the kinetic energy of the ith electron in the dot, C denotes the total capacitance of the gate capacitor and the tunneling junction, and $(Ne)^2/2C = Q^2/2C$ with $Q = Ne$ being the total charge in the dot. Since μ_{N+1} is the minimum energy required for adding the Nth electron, it will be added to the dot as long as μ_{N+1} is below both μ_S and μ_D. In a similar way, addition of one extra electron to a dot having N electrons is possible whenever the electrochemical potential satisfies $\mu_{N+1} = \mu_N + e^2/C + \Delta E$, where $\Delta E = E_{N+1} - E_N$ is lower than both μ_S and μ_D. Thus, the $N+1$ electron should have energy larger than the one for Nth electron by $e^2/C + \Delta E$. The first term $e^2/C = E_c$, representing the energy required to overcome the Coulomb repulsion among different electrons, is called charging energy and the second term ΔE is the result of quantized electron energy levels of the dot.

For the case with $\mu_{N+1} > \mu_S, \mu_D > \mu_N$ (case 1), all the levels below μ_N represent filled levels, while those above μ_{N+1} are empty. The lowest unoccupied level μ_{N+1} cannot be occupied by electrons since it is above the Fermi levels of both electrodes. Therefore the current is "blocked" due to the charge addition energy and the dot is stable with N electrons. In another case with $\mu_D > \mu_{N+1} > \mu_S$ (case 2), the $N+1$th electron can be added from the drain and then it can flow to the source electrode, thus allowing electric current to flow by constantly switching the charge state of the dot between N and $N+1$. As the gate voltage V_G is increased, the electrochemical potential of the dot changes linearly with V_G and this allows one to change the number of electrons on the dot. The conductance (G) as a function of V_G at low bias is illustrated in Figure 4 and shows a series of peak (on-state) as well as valleys of low conductance (off-state). In the valleys, the number of electronics on the dot is fixed (N, $N+1$, $N+2$ and so on) and the current is blocked by the charge addition energy $e^2/C + \Delta E$ (case 1). The peaks in the conductance curve (case 2), known as Coulomb oscillations, indicate that the dot carrying current by oscillating between two adjacent charge states. However, the thermal energy should be ensured small enough to produce Coulomb oscillations, i.e.,

$$e^2/C + \Delta E \gg k_B T\,. \tag{2}$$

For large thermal fluctuations, the Coulomb oscillations will disappear. Secondly, the contact resistance between the dot and two leads need to be larger than the resistance of a single conductance channel, that is,

$$R_{contact} \gg h/e^2 \sim 25.81\,k\Omega\,. \tag{3}$$

Many different systems exhibit single electron transport behavior, which include metallic nanoparticles (24), single-molecule transistors incorporating trimetal molecules (25), carbon nanotubes (26; 27), semiconducting nanocrystals (28) and single molecules (29; 30).

By including the coupling λ_c of a quantum dot to two electrodes, Eq. (1) is modified to (31)

$$\mu_{N+1} = E_{N+1} + \frac{(N+1/2)e^2}{C} + \lambda_c\,\rho_L\,, \tag{4}$$

where ρ_L is the average linear electron density of one-dimensional electrodes. Here, the resonant levels $\{\mu_{N+1}\}$ will depend on the electrode chemical potential μ_0 only through the linear electron density ρ_L. Therefore,, we get

$$\frac{\partial\mu_{N+1}(\mu_0)}{\partial\mu_0} = \lambda_c\,\frac{\partial\rho_L(\mu_0)}{\partial\mu_0} \equiv \lambda_c\,g_{1D}(\mu_0)\,. \tag{5}$$

By choosing the bottom of the electronic energy dispersion as the energy reference point, then the gate potential eV_g can be regarded as the difference $\delta\mu_0$ between the fixed chemical potential of the conductive substrate and μ_0. Therefore, we can set $\delta\mu_0 = \gamma e\,\delta V_g$, where $\gamma < 1$ is a ratio parameter determined by the self-consistent calculation.

Let ν_N be the value of the electrode chemical potential which is in resonance with the level μ_N of the quantum dot. Then we obtain the self-consistent equation $\nu_N = \mu_N(\nu_N)$, and the period of V_G (or μ_0) in the conductance oscillations will be given by

$$\delta\mu_0 = \nu_{N+1} - \nu_N = \Delta E + \frac{e^2}{C} + \lambda_c\,[\rho_L(\nu_{N+1})$$

$$-\rho_L(\nu_N)] = \Delta E + \frac{e^2}{C} + \lambda_c\,g_{1D}(\mu_0)\delta\mu_0\,, \tag{6}$$

or equivalently by

$$\delta\mu_0 = \frac{\Delta E + e^2/C}{1 - \lambda_c\,g_{1D}(\mu_0)} \equiv \frac{\Delta E + e^2/C}{\mathcal{K}(\mu_0)} = \gamma e\,\delta V_G \tag{7}$$

with $\mathcal{K}(\mu_0) = 1 - \lambda_c\,g_{1D}(\mu_0)$ being the screening factor to the charge addition energy by coupling with one-dimensional electron gases. Here, the coupling constant λ_c of the quantum dot can be estimated by

$$\lambda_c \sim \frac{e^2}{4\pi\epsilon_0\epsilon_{\rm eff}L_0}\left[\frac{3}{2} + \ln\left(\frac{L_0}{W_0}\right)\right] \equiv \frac{e^2}{C_0}\,, \tag{8}$$

where L_0 and W_0 are associated with the gate length and the chain width, respectively, and $\epsilon_{\rm eff}$ is the effective dielectric constant of the quantum dot. From this we know that C_0 is just the bare dot capacitance and roughly proportional to L_0 and weakly depends on the chain width as is expected.

For a non-interacting one-dimensional electron gas, the density of states per unit length can be calculated as

$$g_{\rm 1D}(\mu_0) = \frac{\sqrt{2m^*}}{\pi\hbar} \sum_{j=1}^{\rm occupied} \frac{1}{\sqrt{\mu_0 - \varepsilon_j}} \,, \qquad (9)$$

where m^* is the effective mass of the electrons, and ε_j is the bottom of the jth subband. Since $\delta g_{\rm 1D}(\mu_0)/g_{\rm 1D}(\mu_0) = \delta V_{\rm G}/[2(V_{\rm G} - V_{\rm th})]$, we can approximate $g_{\rm 1D}(\mu_0)$ as a constant in a range much smaller than $V_{\rm G} - V_{\rm th}$, where $V_{\rm th}$ is the threshold gate voltage, related to the bottom of the lowest subband energy dispersion. Furthermore, from Eqs. (5) and (7) we can get

$$\frac{\partial \mu_{N+1}(\mu_0)}{\partial \mu_0} = \lambda_{\rm c}\, g_{\rm 1D}(\mu_0) = 1 - \mathcal{K}(\mu_0) \,. \qquad (10)$$

Finally, for finite temperatures $T > 0$, by assuming that the observed conductance peaks can be attributed to the many-body resonant tunneling mechanism (32) through the resonant levels $\{\mu_N\}$, we can write down the conductance G with the help of Landauer-type formula (33)

$$G(\mu_0,\, T) = \frac{e^2}{h} \sum_N A_N(\mu_0,\, T)$$

$$\times \cosh^{-2}\left(\frac{\mu_N - \mu_0}{2k_{\rm B}T}\right) \,, \qquad (11)$$

where $A_N(\mu_0,\, T)$, which is proportional to $\lambda_{\rm c}$, represents the effective transmission coefficient through the Nth resonant level, and we have assumed a Fermi-Dirac distribution for the one-dimensional electron gas, the assumption also used for fitting experimental data in Ref. [34].

B. Ballistic Transport

Whenever the mean-free-path of electrons becomes shorter than the reduced molecular-chain length, they will enter into a quantum-ballistic regime. In this case, the ballistic heat ($Q^{(1)}$) and charge ($Q^{(0)}$) currents are given by (35)

$$Q^{(\ell)} = 2(-e)^{1-\ell} \sum_{n,k} \frac{v_{nk}}{\mathcal{L}} (\varepsilon_{nk} - \bar{\mu})^\ell [\theta(-v_{nk}) f^{(0)}_{nk,R}$$

$$\times (1 - f^{(0)}_{nk,L}) + \theta(v_{nk}) f^{(0)}_{nk,L} (1 - f^{(0)}_{nk,R})] \,, \qquad (12)$$

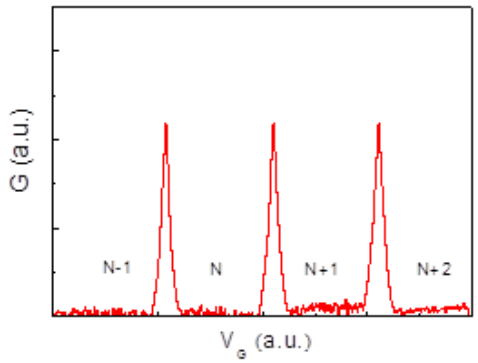

FIG. 4 (Color online) Conductance (G) versus gate bias (V_G) curves displaying Coulomb oscillation. The numbers ($N-1$, N, $N+1, \cdots$, etc) in each conductance valley represents number of electrons on the dot.

where $\ell = 0, 1$, $\mathcal{L}$ is the channel length, $\bar{\mu}$ is the chemical potential in the channel, and $\theta(x)$ is the unit step function. In Eq. (12), n is the sublevel index, k is the wave number of a band, $\varepsilon_{nk} = (n + 1/2)\hbar\Omega_x + \hbar^2k^2/2m^{**}$ represents the nth energy band, $\Omega_x = (\omega_x^2 + \omega_c^2)^{1/2}$, $\hbar\omega_x$ is the sublevel separation in a harmonic-potential model. $\omega_c = eB/m^*$, $m^{**} = m^*/[1-(\omega_c/\Omega_x)^2]$, m^* is the effective mass, B is the applied magnetic field perpendicular to the chain, $v_{nk} = \partial\varepsilon_{nk}/\partial\hbar k$ is the group velocity, and $f^{(0)}_{nk,\alpha}$ is the Fermi-Dirac distribution function for the two-dimensional electrodes on the left ($\alpha = L$) and the right ($\alpha = R$) side, with the chemical potential μ_α. The physical meaning of Eq. (12) is self-evident. Equation (12) can be simplified, in view of $v_{n,-k} = -v_{nk}$ (symmetric band), as

$$Q^{(\ell)} = \frac{2(-e)^{1-\ell}}{\pi}$$

$$\times \sum_n \int_0^\infty dk\, |v_{nk}| (\varepsilon_{nk} - \bar{\mu})^\ell (f^{(0)}_{nk,L} - f^{(0)}_{nk,R}) \,. \qquad (13)$$

Using $\mu_L + eV = \mu_R \equiv \mu$, $f^{(0)}_{nk,L} - f^{(0)}_{nk,R} = eV f^{(0)'}_{nk}$, and $\bar{\mu} \to \mu = \mu_L = \mu_R$ in the limit $V \to 0$, where V is the infinitesimal voltage difference between the left and the right electrodes, we find

$$Q^{(\ell)} = \frac{2eV(-e)^{1-\ell}}{\pi} \sum_n \Big(\int_{\varepsilon_{n,k=0}}^{\varepsilon_{n,k_1}} + \int_{\varepsilon_{n,k_1}}^{\varepsilon_{n,k_2}} + \cdots + \int_{\varepsilon_{n,k^*}}^{\infty} \Big)$$

$$\times {\rm sign}(v_{nk}) (\varepsilon_{nk} - \mu)^\ell \left[\frac{\partial f^{(0)}_{nk}}{\partial \varepsilon_{nk}}\right] d\varepsilon_{nk} \,, \qquad (14)$$

where the lower limit equals the energy $\varepsilon_{n,k=0}$ at $k = 0$. In Eq. (14), the energy integration over the range $0 < k < \infty$ is chopped into the sum of the integrations between the successive extremum points ε_{n,k_m}, where $\varepsilon_{n,k}$ is assumed to be a

monotonic function of k and ε_{n,k^*} is the last extremum (minimum) point. Each integration can be carried out analytically for both $\ell = 0, 1$, yielding the thermoelectric power (TEP) S, given by

$$S = \frac{Q^{(1)}}{TQ^{(0)}} = -\frac{k_{\rm B}}{eF} \sum_n \sum_\gamma C_{n,\gamma} \left[\beta(\varepsilon_{n,\gamma} - \mu)\right.$$

$$\left. \times f^{(0)}(\varepsilon_{n,\gamma}) + \ln(e^{\beta(\mu-\varepsilon_{n,\gamma})} + 1)\right] , \qquad (15)$$

where $\beta = 1/k_B T$ and

$$F = \sum_n \sum_\gamma C_{n,\gamma} f^{(0)}(\varepsilon_{n,\gamma}) . \qquad (16)$$

Here, γ-summation indicates summing over all the energy-extremum points on each curve n ($-\infty < k < \infty$). The quantity $\varepsilon_{n,\gamma}$ is the extremum energy. For a given curve n, $C_{n,\gamma} = 1$ for a local energy minimum point and $C_{n,\gamma} = -1$ for a local energy maximum point. The quantity F equals the number of the pairs of the Fermi points at $T = 0$ and is related to the conductance G by $G = 2e^2F/h$.

The TEP is quantized at $T = 0\,\mathrm{K}$ as $S = -(k_B/e)\ln 2/[G/(2e^2/h)]$ in general at the energy-extremum points $\mu = \varepsilon_{n,\gamma}$ in Eq. (27), where $G = (2e^2/h)(i + 1/2)$ is the zero-temperature quantized ballistic conductance with $i = 1, 2, \cdots$.

We note that m^{**} becomes heavier as B increases, leading to a large density of states. As a result, the sublevels become depopulated successively for increasing B. Figure 5 shows G and S of a conducting molecular chain obtained from Eq. (27) for two temperatures as a function of B when several levels are occupied at $B = 0$. The parameter $\hbar\omega_x$ and the electron density n_{1D} are given in the inset. The TEP is very small when μ lies away from the edges of the sublevels because the contributions to the heat current $Q^{(1)}$ in Eq. (14) from above μ ($\varepsilon_{nk} > \mu$) cancels those from below μ ($\varepsilon_{nk} < \mu$). This cancellation does not occur when μ is within the thermal energy $k_B T$ of the sublevel edges, yielding spikes for the TEP just before a level is depopulated at the knees of the quantum steps of G. These spikes broaden as T is raised. This behavior is similar to the density dependence of the field-free TEP studied earlier (36).

C. Surface-Plasmon Coupling

For photo-excited spin-degenerated electrons in a quantum dot, the semiconductor Bloch equations (37) with $\ell = 1, 2, \cdots$ are given by

$$\frac{dn_\ell^{\rm e}}{dt} = \frac{2}{\hbar} \sum_j {\rm Im}\left[\left(Y_\ell^j\right)^* \left(\mathcal{M}_{\ell,j}^{\rm eh} - Y_\ell^j\, V_{\ell,j;j,\ell}^{\rm eh}\right)\right]$$

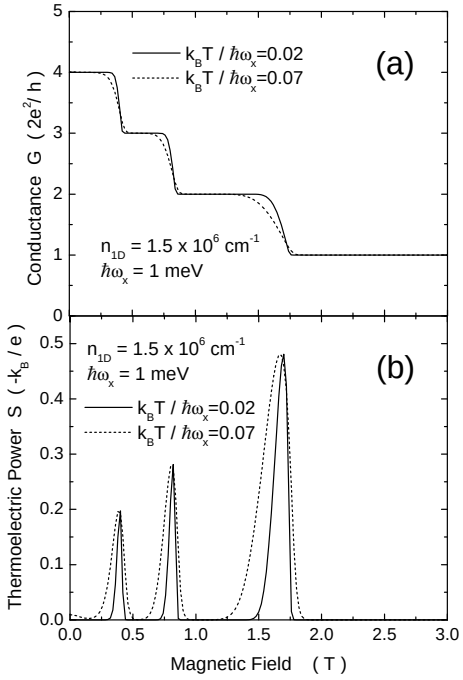

FIG. 5 Ballistic (a) G and (b) S for two temperatures in a single chain with four sublevels occupied initially at $B = 0$. Here, we set $m^* = 0.067\, m_e$ with free-electron mass m_e. Other parameters are directly given in the figure.

$$+ \left.\frac{\partial n_\ell^{\rm e}}{\partial t}\right|_{\rm rel} - \delta_{\ell,1}\, \mathcal{R}_{\rm sp}\, n_1^{\rm e}\, n_1^{\rm h} , \qquad (17)$$

where $\mathcal{R}_{\rm sp}$ is the spontaneous emission rate and $n_\ell^{\rm e}$ represents the electron level population. In Eq. (17), the term marked 'rel' is the non-radiative energy relaxation (38) for $n_\ell^{\rm e}$, and the Y_ℓ^j, $\mathcal{M}_{\ell,j}^{\rm eh}$, and $V_{\ell,j;j,\ell}^{\rm eh}$ terms are given later in this subsection. Similarly, for spin-degenerate holes in a quantum dot, the semiconductor Bloch equations with $j = 1, 2, \cdots$ are found to be

$$\frac{dn_j^{\rm h}}{dt} = \frac{2}{\hbar} \sum_\ell {\rm Im}\left[\left(Y_\ell^j\right)^* \left(\mathcal{M}_{\ell,j}^{\rm eh} - Y_\ell^j\, V_{\ell,j;j,\ell}^{\rm eh}\right)\right]$$

$$+ \left.\frac{\partial n_j^{\rm h}}{\partial t}\right|_{\rm rel} - \delta_{j,1}\, \mathcal{R}_{\rm sp}\, n_1^{\rm e}\, n_1^{\rm h} , \qquad (18)$$

where $n_j^{\rm h}$ stands for the hole energy level population. Again, the non-radiative energy relaxation for $n_j^{\rm h}$ is incorporated in Eq. (18). Finally, for spin-averaged e-h plasmas, the induced interband optical coherence, which is introduced in Eqs. (17) and (18), with $j = 1, 2, \cdots$ and $\ell = 1, 2, \cdots$ satisfies the following equations,

$$i\hbar \frac{d}{dt} Y_\ell^j = \left[\bar{\varepsilon}_\ell^{\rm e}(\omega) + \bar{\varepsilon}_j^{\rm h}(\omega) - \hbar(\omega + i\gamma_0)\right] Y_\ell^j$$

$$+\left(1-n_\ell^{\rm e}-n_j^{\rm h}\right)\left(\mathcal{M}^{\rm eh}_{\ell,j}-Y_\ell^j\,V^{\rm eh}_{\ell,j;j,\ell}\right)+Y_\ell^j\left[\sum_{j_1} n^{\rm h}_{j_1}\right.$$

$$\left.\times\left(V^{\rm hh}_{j,j_1;j_1,j}-V^{\rm hh}_{j,j_1;j,j_1}\right)-\sum_{\ell_1} n^{\rm e}_{\ell_1}\,V^{\rm eh}_{\ell_1,j;j,\ell_1}\right]+Y_\ell^j\left[\sum_{\ell_1} n^{\rm e}_{\ell_1}\right.$$

$$\left.\times\left(V^{\rm ee}_{\ell,\ell_1;\ell_1,\ell}-V^{\rm ee}_{\ell,\ell_1;\ell,\ell_1}\right)-\sum_{j_1} n^{\rm h}_{j_1}\,V^{\rm eh}_{\ell,j_1;j_1,\ell}\right]\,, \qquad (19)$$

where $\hbar\gamma_0 = \hbar\gamma_{\rm eh} + \hbar\gamma_{ext}$ is the total energy-level broadening due to both the finite carrier lifetime and the loss of an external evanescent field, ω is the frequency of the external field, and $\overline{\varepsilon}^{\rm e}_\ell(\omega)$ and $\overline{\varepsilon}^{\rm h}_j(\omega)$ are the kinetic energies of dressed single electrons and holes, respectively. (37) In Eq. (19), the diagonal dephasing (γ_0) of Y_ℓ^j, the renormalization of interband Rabi coupling ($Y_\ell^j\,V^{\rm eh}_{\ell,j;j,\ell}$), the renormalization of electron and hole energies (third and fourth terms on the right-hand side), as well as the exciton binding energy, are all taken into consideration.

The steady-state solution to Eq. (19), i.e. under the condition of $dY_\ell^j/dt = 0$, is found to be

$$Y_\ell^j(t|\omega) = \left[\frac{1-n^{\rm e}_\ell(t)-n^{\rm h}_j(t)}{\hbar(\omega+i\gamma_0)-\hbar\overline{\Omega}^{\rm eh}_{\ell,j}(\omega|t)}\right]\mathcal{M}^{\rm eh}_{\ell,j}(t)\,, \qquad (20)$$

where the photon and Coulomb renormalized interband energy-level separation $\hbar\overline{\Omega}^{\rm eh}_{\ell,j}(\omega|t)$ is given by

$$\hbar\overline{\Omega}^{\rm eh}_{\ell,j}(\omega|t) = \overline{\varepsilon}^{\rm e}_\ell(\omega|t)+\overline{\varepsilon}^{\rm h}_j(\omega|t)-V^{eh}_{\ell,j;j,\ell}$$

$$+\sum_{\ell_1} n^{\rm e}_{\ell_1}(t)\left(V^{\rm ee}_{\ell,\ell_1;\ell_1,\ell}-V^{\rm ee}_{\ell,\ell_1;\ell,\ell_1}\right)$$

$$+\sum_{j_1} n^{\rm h}_{j_1}(t)\left(V^{\rm hh}_{j,j_1;j_1,j}-V^{\rm hh}_{j,j_1;j,j_1}\right)$$

$$-\sum_{\ell_1\neq\ell} n^{\rm e}_{\ell_1}(t)\,V^{\rm eh}_{\ell_1,j;j,\ell_1}-\sum_{j_1\neq j} n^{\rm h}_{j_1}(t)\,V^{\rm eh}_{\ell,j_1;j_1,\ell}\,. \qquad (21)$$

The Coulomb interaction matrix elements introduced in Eqs.(17), (18) and (19) are calculated as

$$V^{\rm ee}_{\ell_1,\ell_2;\ell_3,\ell_4} = V_0\int\frac{d^2\mathbf{q}_\parallel}{q_\parallel}\,\mathcal{F}^{\rm e}_{\ell_1,\ell_4}(\mathbf{q}_\parallel)\,\mathcal{F}^{\rm e}_{\ell_2,\ell_3}(-\mathbf{q}_\parallel)\,, \qquad (22)$$

$$V^{\rm hh}_{j_1,j_2;j_3,j_4} = V_0\int\frac{d^2\mathbf{q}_\parallel}{q_\parallel}\,\mathcal{F}^{\rm h}_{j_1,j_4}(\mathbf{q}_\parallel)\,\mathcal{F}^{\rm h}_{j_2,j_3}(-\mathbf{q}_\parallel)\,, \qquad (23)$$

$$V^{\rm eh}_{\ell,j;j',\ell'} = V_0\int\frac{d^2\mathbf{q}_\parallel}{q_\parallel}\,\mathcal{F}^{\rm e}_{\ell,\ell'}(\mathbf{q}_\parallel)\,\mathcal{F}^{\rm h}_{j,j'}(-\mathbf{q}_\parallel)\,, \qquad (24)$$

where $V_0 = e^2/8\pi^2\epsilon_0\epsilon_b$, the two dimensionless form factors, $\mathcal{F}^{\rm e}_{\ell,\ell'}(\mathbf{q}_\parallel)$ and $\mathcal{F}^{\rm h}_{j,j'}(\mathbf{q}_\parallel)$, are introduced in Eqs. (22)-(24) for electrons and holes due to quantum confinement by a disk-like quantum dot. In addition, the matrix elements employed in Eqs. (17), (18) and (19) for the Rabi coupling between photo-excited carriers and an evanescent electromagnetic field $\boldsymbol{E}(\mathbf{r};\,t) = \theta(t)\,\boldsymbol{E}(\mathbf{r};\,\omega)\,e^{-i\omega t}$ are given by

$$\mathcal{M}^{\rm eh}_{\ell,j}(t) = -\delta_{\ell,1}\,\delta_{j,1}\,\theta(t)\,\left[\boldsymbol{E}^{\rm eh}_{\ell,j}(\omega)\cdot\mathbf{d}_{\rm c,v}\right]\,, \qquad (25)$$

where $\theta(x)$ is a unit step function, $\mathbf{d}_{\rm c,v}$ is static interband dipole moment, and the effective electric field coupled to the quantum dot is

$$\boldsymbol{E}^{\rm eh}_{\ell,j}(\omega) = \int d^3\mathbf{r}\,[\psi^{\rm e}_\ell(\mathbf{r})]^*\,\boldsymbol{E}(\mathbf{r};\,\omega)\,\left[\psi^{\rm h}_j(\mathbf{r})\right]^*\,. \qquad (26)$$

with $\psi^{\rm e}_\ell(\mathbf{r})$ and $\psi^{\rm h}_j(\mathbf{r})$ being the electron and hole wave functions, respectively, in the quantum dot.

Using the Green's function (39) $\mathcal{G}_{\mu\nu}(\mathbf{r},\mathbf{r}';\,\omega)$, we can convert the Maxwell equation into a three-dimensional integral equation for $\mu,\,\nu = 1,\,2,\,3$

$$E_\mu(\mathbf{r};\,\omega) = E^{(0)}_\mu(\mathbf{r};\,\omega)$$

$$-\frac{\omega^2}{\epsilon_0 c^2}\sum_\nu\int d^3\mathbf{r}'\,\mathcal{G}_{\mu\nu}(\mathbf{r},\mathbf{r}';\,\omega)\,\mathcal{P}^{\rm loc}_\nu(\mathbf{r}';\,\omega)\,, \qquad (27)$$

where $E^{(0)}_\mu(\mathbf{r};\,\omega)$ is an incident surface-plasmon (SP) field. The photo-induced interband optical polarization $\boldsymbol{\mathcal{P}}^{\rm loc}(\mathbf{r};\,\omega)$, which is related to the induced interband optical coherence, by dressed electrons in the quantum dot is given by (40)

$$\boldsymbol{\mathcal{P}}^{\rm loc}(\mathbf{r};\,\omega) = 2\,|\xi(\mathbf{r})|^2\,\mathbf{d}_{\rm c,v}\left\{\int d^3\mathbf{r}'\,\psi^{\rm e}_1(\mathbf{r}')\,\psi^{\rm h}_1(\mathbf{r}')\right\}$$

$$\times\frac{1}{\hbar}\lim_{t\to\infty}\left[\frac{1-n^{\rm e}_1(t)-n^{\rm h}_1(t)}{\omega+i\gamma_0-\overline{\Omega}^{\rm eh}_{1,1}(\omega|t)}\right]\mathcal{M}^{\rm eh}_{1,1}(t)\,, \qquad (28)$$

where $\hat{\mathbf{e}}_{\rm d}$ is the unit vector of the dipole moment and the profile function $|\xi(\mathbf{r})|^2$ comes from the confinement of a quantum dot.

Figure 6 presents the quantum dot absorption coefficient $\beta_0(\omega_{\rm sp})$ for a surface-plasmon field, the scattered field $|\mathbf{E}_{\rm tot}-\mathbf{E}_{\rm sp}|$ of the SP field, and the energy-level occupations for electrons $n_{\ell,e}$ and holes $n_{j,h}$ with $\ell,\,j\,=\,1,\,2$ as functions of frequency detuning $\Delta\hbar\omega_{\rm sp}\,\equiv\,\hbar\omega_{\rm sp}\,-\,(E_{\rm G}\,+\,\varepsilon_{1,e}\,+\,\varepsilon_{1,h})$.

A dip is observed at resonance $\Delta\hbar\omega_{\rm sp} = 0$ in the upper-left panel, which appears to become deeper with decreasing amplitude $E_{\rm sp}$ of the SP field in the strong-coupling regime due to a decrease in the saturated absorption. However, this dip completely disappears when $E_{\rm sp}$ drops to 25 kV/cm in the weak-coupling regime due to the suppression of the photon-dressing effect, which is accompanied by an order of magnitude increase in the absorption-peak strength. The dip in the upper-left panel corresponds to a peak in the scattered field, as can be seen from the upper-right panel of Fig. 6. The scattered field increases with frequency detuning away from resonance, corresponding to the decreasing absorption. As a result, a minimum appears on each side of the resonance in the scattered field in the strong-coupling regime. The Maxwell-Bloch equations couple the field dynamics outside of a quantum dot with the electron dynamics inside the dot. At $E_{\rm sp} = 125$ kV/cm in the lower-right panel, we find peaks in the energy-level occupations at resonance, which are broadened by the finite carrier lifetime as well as the optical power of the SP field. Moreover, jumps in the energy-level occupations can be seen at resonance due to Rabi splitting of the energy levels in the dressed electron states. The effect of resonant phonon absorption also plays a significant role in the finite value of $n_{2,e}$ with energy-level separations $\varepsilon_{2,e} - \varepsilon_{1,e}$ approximately equals to the optical phonon energy. However, as $E_{\rm sp}$ decreases to 25 kV/cm in the lower-left panel, peaks in the energy-level occupations are greatly sharpened and negatively shifted due to the suppression of the broadening from the optical power and the excitonic effect, respectively. Additionally, jumps in the energy-level occupations become invisible because the Rabi-split energy gap in this case is much smaller than the energy-level broadening from the finite lifetime of electrons (i.e. severely damped Rabi oscillations between the first electron and hole levels).

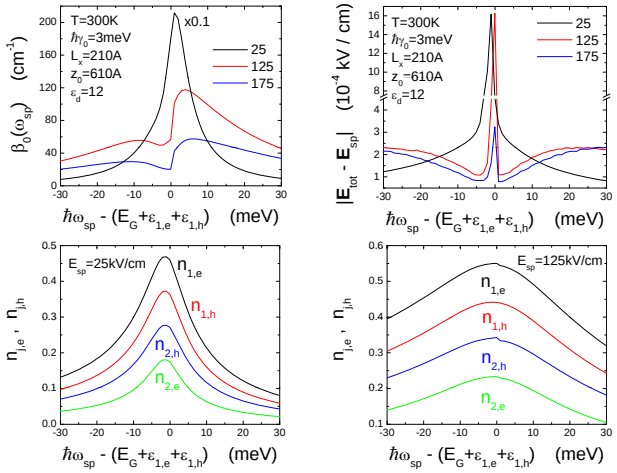

FIG. 6 Optical absorption coefficients $\beta_0(\omega_{\rm sp})$ (upper-left panel) and scattering field $|\mathbf{E}_{\rm tot} - \mathbf{E}_{\rm sp}|$ at the quantum dot (upper-right panel), as well as the energy-level occupations for electrons $n_{\ell,e}$ and holes $n_{j,h}$ (lower panels) with ℓ, $j = 1$, 2, as functions of the frequency detuning $\Delta\hbar\omega_{\rm sp} \equiv \hbar\omega_{\rm sp} - (E_{\rm G} + \varepsilon_{1,e} + \varepsilon_{1,h})$. Here, the results for various amplitudes $E_{\rm sp}$ of an SP field with frequency $\omega_{\rm sp}$ are presented in the upper panels, along with a comparison of the energy-level occupations for $E_{\rm sp} = 25$ and 125 kV/cm in the lower panels. The label $\times 0.1$ in the upper-left panel indicates that the result is multiplied by a factor of 0.1.

V. EFFECT OF EXTERNAL PARAMETERS

The conductance of a single molecule is affected significantly by several external parameters which may cause a change in the local charge distribution, distortion in molecular structure or the electronic states of the molecule producing difference in the molecular conductance. A few of these external parameters are listed below.

A. Mechanical Force

The force applied in a molecular junction may distort the molecular structure and hence change the electronic states of the molecule producing a difference in the conductivity levels. The effect is more pronounced for softer molecules like oligothiophenes, since the strong coupling between the electronic states and the molecular structures causes a large change in the conductance (41). Secondly, during the breakdown of the molecular junctions the conductance traces although seemed flat, careful examination shows a finite decrease (10-20% decrease for alkanedithiols) in the conductance upon stretching (41). Thirdly, a small molecule cannot be stretched without tearing to that limit which a molecular junction can withstand (several angstroms).

B. Environment Effect

The molecular conductance is also a function of the local environment, such as, metal ions, solvent molecules, and solution pH. The presence of metal ions in solution produce strong binding of the ions to the molecule inducing conformational changes of the molecule and hence change in the conductance of the molecule (2). Even the solution pH can change the electronic states of a molecule resulting significant decrease in the conductance of the molecule with increase in solution pH (42).

C. Local-Heating (Joule) Effects

In ultra-small scale electronic devices, local heating effect due to current flow and heat dissipation is a crucial factor. Large current density in the junction can produce substantial heat. During inelastic electron transport in nanoscale junction, although a small amount of electron energy contributes to emission of phonons (43; 44), it may still induce appreciable local heating effect (45). An increase in temperature by $\sim$ 25 K above room temperature was observed for octanedithiol at bias of 1 V.

D. Energy Level Alignment of Molecule

The alignment of the molecular energy levels, i.e., highest occupied molecular orbital (HOMO) and the lowest unoccupied molecular orbital (LUMO), with the Fermi levels of the metal contacts determine the conductance of a molecule. A molecule exhibits very low conductance if it has a large HOMO-LUMO gap ($\sim 5\,eV$) in the neutral state. Because, in that case, the Fermi level of the electrode will most likely be positioned within the gap and thee will not be any transfer of electrons from the electrode to the molecule. On the other hand, spontaneous oxidation/reduction of the molecules and the easy transfer of electrons from one electrode to other takes place if HOMO/LUMO level is aligned with the metal Fermi level leading to high conductance. It is often very difficult to determine the interactions between the molecules and the electrode, although, STM tunneling spectroscopy has been used to study the electronic states of molecules absorbed on the surfaces to resolve different molecular energy levels and their relative positions to the Au Fermi level (46; 47). The electrochemical gate control of the conductance of several single redox molecules has also been observed (48; 49).

E. Mechanically Controllable Break Junction (MCBJ)

As shown in Figure 7, the distance between two atomically sharp metallic nanocontacts is easily adjusted by mechanically breaking a metal wire. The electrical conductance of self-assembled molecular (SAM) monolayers bridging the junction (50; 51) is measured by bringing the tips close to each other with a voltage bias between them while slowly breading the contacts. The molecular conductance varies as a result of variation of the electrode gap due to the bending of a common bendable substrate mounting the two wire ends, and the junction becomes insensitive to the external vibrations. A stressed or deformed junction results in different configurations and hence different electronic properties of the molecular species. Due to the high stability of MCBJ, the same junction can be investigated repeatedly to obtain a large amount of information on a molecule with the systematic variation of control parameters such as temperature and magnetic field. Although both electrodes are made of the same metal, and one cannot assume these are truly symmetric junctions. The reason for that is because of dimensional control at the atomic level. Random variation is geometrical structural shapes is the obvious drawback of existing techniques. Also, the differences in the sharpness of the broken tips may cause large variation in the electric filed around the broken ends of the wires as well as heat may be generated from the undesirable motion of the mechanical drive used in this technique. The MCBJ technique is not found to be suitable for the measurement on highly integrated molecular electronic devices. However, the lithographically patterned MCBJs have been very useful for the investigation of molecular conductance of such systems and do not require ultra-high vacuum and highly cleaned conducting substrates.

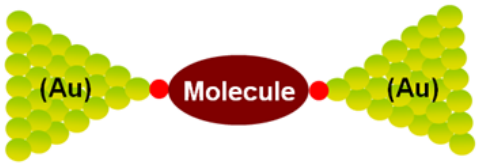

FIG. 7 (Color online) Schematics of MCBJ. The molecular monolayer is connected with the two Au electrodes via a chemical bond through thiol end groups.

VI. PREPARATION OF SELF-ASSEMBLED MONOLAYERS (SAM)

For fabrication of molecular junction, the break junction is submerged in the solution of the molecule with desired concentration for an extended amount of time; and the molecules are then self-assembled onto both of the metallic tips because of functionalization of the molecules at both ends binding with the metal. The residual molecules which are not involved in chemical bonds with the tips may be washed away with distilled water. The nanolayers of organic molecules are uniformly chemisorbed over the metal contacts though slow evaporation of solvents. The presence of deformities in the layer, such as separation of molecules due to excessive tilt or holes in the layer, may cause undesirable electrical short between the electrodes. Alkanethiols on atomically cleaned and polished gold substrate was commonly used as SAM (52; 53) because of easy formation of stable monolayers as well as having varieties of potential applications such as sensors, corrosion inhibition, wetting control and molecular electronic devices (54; 55). The nanogap formed as a result of breaking in an MCBJ, is spanned by one or few molecules during SAM preparation, thus allowing one to measure single molecular conductance. Schematic representation of a self-assembled monolayer on Au substrate is shown in the inset of Figure 8(a).

Typical current-voltage (I-V) characteristics of the SAM layer on gold (Au) substrate of a dithiol NOPE molecule comprised of the same NO_2 functionalized OPE oligo (phenyleneethynylene) NOPE molecules are shown in Figure 8(a) at three different temperatures of $100\,K$, $200\,K$ and $300\,K$. The molecule showed stable and reproducible I-V characteristics allowing multiple scans. The differential conductance of the molecule, calculated from the I-V curves with a resistance of $2.1/1\,M\Omega$ being measured at $300\,K$ for the voltage scan of $\pm 1\,V$ through $0\,V$, was found to be asymmetric and is shown in Figure 8(b). This observation may be attributed to uneven strength in electrically coupling between the metal tips (56). It is clear from the figure that the high conductance region moves to higher voltage when the temperature is decreased. This implies that a thermal mechanism may be responsible for the sudden increase in current (57).

$1,4$ Benzene-dithiol (BDT) SAM in gold break junction (51) displayed nearly symmetric differential conductance a limited asymmetry at room temperature for relatively high bias within the bias range $\pm 4\,V$. Theoretical studies of the BDT/Au break-junction have yielded almost similar re-

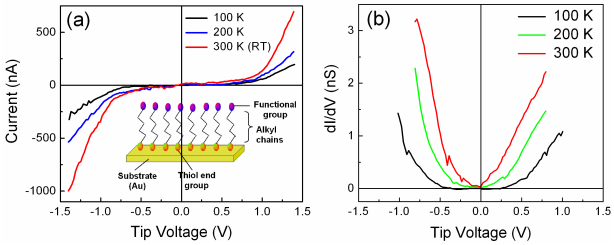

FIG. 8 (Color online) (a) I-V characteristics of dithiol NOPE molecule measured in the break junction set-up at different temperatures. Inset: schematic representation of a self-assembled monolayer on Au substrate. (b) Differential conductance of the same molecule calculated from data (a).

sults (58; 59) with symmetric conductance curves. Significant enhancement in differential conductance of the junction was found to increase strongly from low to high voltage regimes. This behavior was ascribed to the fact that the Fermi level of Au contacts fall within the HOMO-LUMO gap of the molecule at low bias. However, transport through resonant states of the molecular hybridized with the metal tips increased conductance at higher biases. However, experimentally measured current values disagree with that of theoretical calculation (58; 59).

The conductance of quantum point contact (a single metal atom or a row of atoms of the same metal as of the electrodes) (60; 61) is usually expressed in units of $G_0 = 2e^2/h$ (e = electronic charge, h = Planck constant) as at higher biases, a measure of the transmission of electrons through the point contact. The contact size of the order of electron Fermi wavelength for electrons in Au is only a few Å (for Au, $G_0 = 77.4\,\mu S$), the appearance of conductance quantization (62) indicates the formation of an atomic-scale contact between the tip and the substrate with lowest step corresponds to a single molecule bridging the two electrodes. In an earlier experiment based on MCBJ at low temperatures, the conductance is found to be quantized in units of G_0 as a function of contact elongation (elongation speed being in the range of 1-10 pm/s) for four different materials (Al, Au, Pb and Nb) (63). The average conductance as a measure by MCBJ method for $1,4$ benzene-dithiol (BDT) molecule was $0.0099\,G_0$ in case of dithiol NOPE molecule. A summary of the present study including the chemical structures of the molecule is presented in Table 1.

Table 1: Summary of Molecules

Molecule	Average Conductance	Technique used	Chemical Structure	Application [Reference]
1,4 benzene-dithiol (BDT)	0.0099 G_0 (at RT) **[$G_0 = 2e^2/h$]**	(MCBJ)	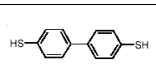	Molecular wire [18, 25]
dithiol NOPE molecule	0.0007 G_0 (at RT)	(MCBJ)	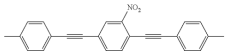	Single molecule device [23, 24]
Copper (II) phthalocyanine	0.00146 G_0 (at RT)	STM	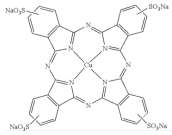	Molecular rectifier [9]
Fluorone dye (Rose Bengal)	0.00161 G_0 (at RT)	STM	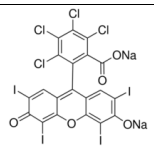	Molecular rectifier [9]
Pentacene	N.A.	AFM	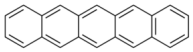	
Fullerenol (C_{60})	0.00142 G_0 (at RT)	Hg blob		Molecular memory [10]
C_{140}	0.2 µS (measured at 1.5 K)	STM	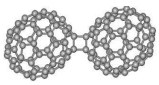	Single electron transistor [79]
double stranded - DNA	10^{-5} – 10^{-6} G_0	STM break junction	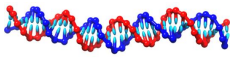	Molecular conduction [2]
C-8 dithiol SAM C-8 monothiol SAM	$9.3 \pm 1.8 \times 10^{-4}$ A/cm^2 (at 1 V) $3.1 \pm 1 \times 10^{-4}$ A/cm^2 (at 1 V)	Inelastic electron tunnelling spectroscopy		Molecular electronic device [8]
$C_{16}H_{33}Q$-3CNQ	0.266 µS	Metal-film-metal sandwich structure	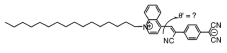	Molecular diode [9]
divanadium molecule [(N,N´,N´´-trimethyl-1,4,7-triazacyclononane)$_2$V$_2$(CN)$_4$(µ-C_4N_4)]	N.A.	STM	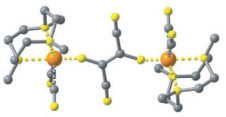	Single molecule magnet [16]
$La_{0.7}Sr_{0.3}MnO_3$/ Alq_3/Co junction	N.A.	Nanoscale cross junction		Organic spin valve/molecular magnet [17]
λ-DNA (as test structure)	N.A.	Solid state nanopore		Single molecule biosensor [22]
$FcC_{11}S$-SAM On Au substrate	N.A.	STM		Negative differential resistance [50]
DNA	N.A.	AFM		Self-assembled periodic nanostructure [48]
Oligothiophenes	7.5×10^{-5} G_0 (for 4T) 2.8×10^{-5} G_0 (for 3T)	c-AFM	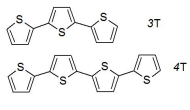	Molecular switch [54]
Metalloprotein (azurin)	N.A.	Electrochemically gated transistor		Bio-electronics [94]

VII. MOLECULAR IMAGING METHODS

A. Scanning Probe Microscope (SPM)

Since the scanning tip remain at a distance from the surface under investigation, no chemical bond is formed between the tip and the surface giving rise to a strongly asymmetric configuration of the electrochemical potentials of the system. The technique has often been used to directly visualize electrochemical processes *in-situ* at the molecular levels for organic monolayers (64; 65). In order to determine single molecular

conductance by SPM technique, the molecule is covalently bonded to the two probing electrodes and the measurement is performed under ultra-clean and ultra-high vacuum environment.

B. Scanning Tunneling Microscope (STM)

STM provides a three-dimensional profile of the investigating surface for quantitative determination of surface roughness, surface defects, the size and conformation of molecules and molecular aggregates with atomic precision or even in subatomic resolution (66). When a sharp tip of an atomic dimension in practice is brought sufficiently close to a substrate adsorbing the molecule, a strong interaction is established between the electron clouds of the surface and tip atoms promotes tunnelling of electrons under a small bias. The exponential variation of current with tip-sample distance leads to mapping the surface image sample with an atomic resolution when scanned over the two-dimensional surface. The basic set up a STM is shown in Figure 9(a) with two piezo-electric scanners to control the position of the tip over the surface. The constant density of states contours is mapped in constant current mode, by adjusting the tip-sample distance with the use of a feedback loop. Alternatively, the vertical position of the tip (z-coordinate) can be held constant to record tunnelling current for mapping the actual density of states. The typical arrangements of the Si atoms can clearly be seen from the ultra-high vacuum STM image of a Si $(111)\,7\times7$ reconstructed surface in Figure 9(b). In this method, the tip-molecule contact is often less well defined than the molecule-substrate contact preventing one from determining the absolute conductance of the molecule. Figure 9(c) illustrates an alternative method in which the molecule is adsorbed onto one end of the substrate and an organic surfactant coated Au nanoparticles are covalently bonded to its other end (67). Electron tunnelling from tip to the substrate exhibits the Coulomb blockade effect due to the presence of the nanoparticles as Coulomb islands (45). Measured I-V curves are interpreted in terms of the Coulomb blockade model to determine the conductance of the molecule (68; 69).

This method has been successfully exploited for the characterization of organic monolayers, polypeptides, biomolecules like DNA, biological tissues and metallic-protein. There have been several reports of STM imaging of DNA molecules embedded in metal films (70), protein characterization by electrochemical techniques (71), studying and investigations of electron transfer in metallic-proteins (72; 73). The conductivity measurement of DNA by STM has been employed to examine the electrical behaviour of DNA as insulators (74), conductors (75), semiconductors (76) and superconductor (77). Additionally, the study of electron transport through DNA (78), DNA array detection may be accomplished using site specific nanoparticles probes (79), self-assembly of two-dimensional DNA crystal (**?**), controlled manipulation of atoms on given surfaces for application as electronic ink (64) and the possibility of designing the catalysis process at the single molecule level and control of the constituents at the molecular levels (81). These include non-linear current-voltage characteristics with NDR behaviour on redox-active molecular monolayers (82) and study of field effects on electron transport in molecules (83). Spectra of a single molecule namely inelastic Electron Tunneling Spectroscopy (IETS) has also be investigated with a cryogenic STM (84).

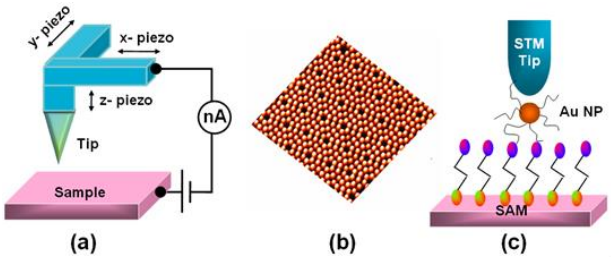

FIG. 9 (Color online) (a) Schematic of STM arrangement with a sharp tip mounted on 3 piezo crystals. x- and y-piezo allow the tip to scan the two-dimensional surface in xy plane while z-piezo controls the tip-sample separation. (b) STM image of a Si $(111)\,7\times7$ surface. Scan area of the image is $15\times15\,\mu m^2$. (c) STM measurement of molecular conductance. One end of the molecule/SAM is attached to the substrate and the other end is bounded to a Au nanoparticle (Au NP).

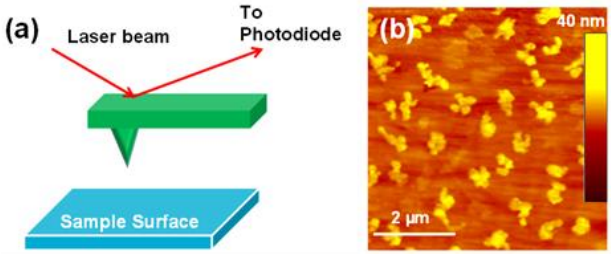

FIG. 10 (Color online) (a) Schematic representation of AFM set up. (b) Tapping mode AFM image of a $2\,nm$ pentacene film grown over a polymer coated glass substrate.

C. Atomic Force Microscope (AFM)

A schematic of the AFM set-up is shown in Figure 10(a). The laser light reflected from the back of the cantilever enters a photodiode/photodetector device. AFM is generally used in tapping mode with the cantilever vibrating above the sample surface and the tip in intermittent contact with the surface. Figure 10(b) shows the tapping mode AFM image of vacuum deposited pentacene film ($2\,nm$) on poly (4-vinyl phenol) (PVP) coated glass substrate. The individual grains of pentacene molecules are seen. Contact mode AFM, where the tip is in contact with the surface continuously, is only used for specific applications, such as force curve measurements. The movement of the tip governed by the tip-surface interactions is measured by detecting the position of a reflected laser beam, focussed onto the back of the cantilever.

AFM can be used to measure different mechanical properties including adhesion strength and magnetic forces and with a conducting tip used in either contact or non-contact mode

of operation (85; 86). This technique offers typically a lower resolution than STM. However, the capability of imaging both conducting and non-conducting surfaces in sub-nanometre level without the need for any additional sample preparation has made AFM more powerful tool than STM for in-situ measurements and real time imaging of biological and chemical processes (87; 88).

D. Conducting Atomic Force Microscope (C-AFM)

In this mode, a platinum or platinum/iridium coated AFM tip is employed for contact to the molecular monolayer with a view to measuring in-situ the current-voltage characteristics. Topographic images may also be recorded using the Pico scan controller in another channel. An external bias to the tip is applied to induce an attractive electrostatic force in addition to the adhesion force, controlling the pressure with which the conductive probe pushes into the sample surface. However, accurate measurement of the molecular conductance requires the pressure to be maintained constant [79]. The bimolecular interaction and bond strength have been measured (89) by recording the force by the biomolecule-functionalized AFM tip when brought in contact with another biological surface, via, protein, cell, tissue. Force-distance curves have been used for multiparametric imaging of native proteins and protein complexes in the native unperturbed state and to simultaneous mapping their biophysical and biochemical properties at atomic resolution (90). The variation in tip pressures may modify the overlapping of electronic wave functions and hence the injection barrier, affecting charge carriers injection from electrode to the molecule and a dramatic change in the conductive properties of the sample. Carbon nanotube (CNT) AFM probes are found to be more durable and offer the improved spatial and lateral resolution of the imaging (91). These probes have been used to extract structural information of tissues (92), multiplexed detection of polymorphic sites and detection of haplotypes in DNA fragments and positions of the tagged sequences (**?**). C-AFM has been used to record Conductance switching behaviour and data storage ability of small molecules have been studied using the C-AFM technique (94).

VIII. NANOPORES

A nanopore is basically a tiny hole of molecular dimension between two metal electrodes providing stable and well defined contacts to the molecular monolayer. A nanopore junction is fabricated by growing a low conductivity silicon nitride (SiN) film is on a Si wafer. Selected areas of the wafer are then etched away so as to leave free standing SiN films. A pore having diameter $\sim$ 10-50 nm is then etched through these films (Figure 11). Thin gold film (Au) is evaporated on the bottom of the wafer over which the SAM of molecule of interest is assembled from the other side of the membrane. A top metal contact is then deposited onto the monolayer to record the I-V characteristics of the sandwich device (95).

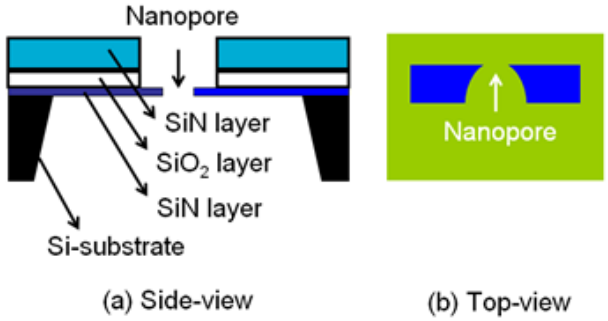

FIG. 11 (Color online) Schematics of nanopore in both (a) side view and (b) top view.

The solid-state nanopore proves to be a versatile single-molecule tool for biophysics and biotechnology applications (96). Ion currents and forces are monitored in nanopore based sensors involving DNA (97), RNA (98; 99) and proteins (100; 101) molecular resolution. Nanopore junction with thioacetatebiphenyl SAM exhibited diode like characteristics (95), while NDR and non-volatile memory switching was observed in nitro-amino benzenethiolate SAM (102).

IX. MERCURY (HG) DROP METHOD

For ultra-thin organic film or organic monolayer, the deposition of a top electrode by thermal evaporation may lead to penetration of highly energetic metallic particles through the film and damage it. Hence, for electrical characterization of SAM of alkanethiol and other molecules Hg-drop method was developed (103). The SAM was either sandwiched between two mercury drops (104) or assembled on a solid substrate, in which case an Hg drop is used as the top electrode (105). Figure 12(a) shows the schematic representation of a simple experimental arrangement where the Hg drop was used as the top electrode. Annealed films were kept in a vacuum chamber ($10^{-3}\,Torr$) at room temperature with the film facing downward. A syringe with a mercury (Hg) drop on its tip was raised from outside the chamber slowly by a micrometre screw till the blob just touched the film. The diameter of the blob was below $0.5\,mm$. The contact between the film and the blob was monitored through a microscope. The bias was applied with respect to the Hg electrode and I-V characteristics were recorded in voltage loops. We have electrically characterized monolayer of a typical D-A system, namely CuPc-fullerenol layer-by-layer electrostatically self-assembled film on Si substrate with Hg blob as the top electrode. Seven consecutive loops are shown in the Figure 12(b). The monolayer was initially in the low-conducting off-state which switched to the high conducting on-state at reverse bias. At any voltage, the current remains at least four orders in magnitude higher as compared to that in the initial scan. The higher level of current is retained even when the bias is scanned in subsequent loops. The switching phenomenon in the monolayer of CuPc:fullerenol is also irreversible in nature making it suitable for WORM memory applications (10). The method is advan-

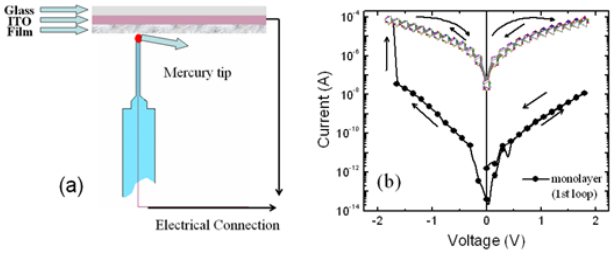

FIG. 12 (Color online) (a) A schematic diagram of the Hg-blob set up for monolayer characterization. (b) I-V characteristics of CuPc:~~fellerenol~~ monolayer on Si with Hg blob as the top electrode under multiple voltage loops. First loop is shown with filled symbol and the subsequent loops are shown with open symbols. Arrows indicate the direction of voltage sweep.

tageous because of its simple design and quick two terminal characterization of SAMs. However, the Hg contacts area is quite large making it difficult to probe single molecular conductance.

X. SUMMARY

The conductance of a single molecule as the conductance depends not only on the intrinsic properties of the molecule, but also on the probing electrodes, electrode-molecule interaction, and its local environment. For unambiguous determination of the molecular conductance, it is essential to fabricate a molecular junction with well-defined contacts at the atomic scale and to carry out the measurement in controlled environment. Despite the challenges, tremendous developments have been made in fabricating different break junction, SPM techniques and nanopore methods. Although, the contact geometries in break junction methods are only little known with insufficient atomic scale structural information, a large number of molecular junctions with different contact geometries can be created allowing one to determine average molecular conductance from the statistical analysis. STM has been efficiently used to create a well-defined metal-molecule-molecule junction with more limited contact areas and to measure the conductance of single molecule. In addition to the single molecule conductance spectra, STM and AFM imaging of single molecule or molecular assemblies and manipulation of atoms by STM have proved SPM a powerful and versatile tool to probe molecules in atomic and even subatomic resolution.

Acknowledgments

This work is sponsored by the Air Force Office of Scientific Research, Air Force Material Command, USAF, under grant number FA 9550-15-1-0123.

References

[1] Sadeghi, H., Sangtarash, S., Lambert, C. J.: “Electron and heat transport in porphyrin-based single-molecule transistors with electro-burnt graphene electrodes”, 2015, Beilstein J. Nanotechnol. **6**, 1413-1420.

[2] Hihath, J., Xu, B., Zhang, P., Tao, N.: “Study of single-nucleotide polymorphisms by means of electrical conductance measurements”, 2005, Proc. Natl. Acad. Sci. **102**, 16979-16983.

[3] Xiao, X., Xu, B., Tao, N.: “Changes in the conductance of single peptide molecules upon metal-ion binding”, 2004, Angew. Chem. Int. Ed. **43**, 6148-6152.

[4] Aviram, A., Ratner, M. A.: “Molecular Rectifier”, 1974, Chem. Phys. Lett. **29**, 277-283.

[5] Xue, Y., Ratner, M.: “Theoretical principles of single-molecule electronics: a chemical and mesoscopic view”, 2005, Int. J. Quantum Chem. **102**, 911-924.

[6] Selzer, Y., Allara, D. L.: “Single-molecule electrical junctions”, 2006, Ann. Rev. Phys. Chem. **57**, 593-623.

[7] Mantooth, B. A., Weiss, P. S.: “Fabrication, assembly, and characterization of molecular electronic components”, 2003, Proc. IEEE **91**, 1785-1802.

[8] Wang, W. Y., Lee, T. H., Reed, M. A.: “Electronic transport in molecular self-assembled monolayer devices”, 2005, Proc. IEEE **93**, 1815-1824.

[9] Metzger, R. M.: “Unimolecular electrical rectifiers”, 2003, Chem. Rev. **103**, 3803-3834.

[10] Mukherjee, B., Pal, A. J.: “Write-once-read-many-times (WORM) memory applications in a monolayer of donor/acceptor supramolecule”, 2007, Chem. Mater. **19**, 1382-1387.

[11] Li, Z., Han, B., Meszaros, G., Pobelov, I., Wandlowski, T. et al.: “Two dimensional assembly and local redox-activity of molecular hybrid structures in an electrochemical environment”, 2006, Faraday Discuss. **131**, 121-143.

[12] Qiu, X. H., Nazin, G. V., Ho, W.: “Mechanisms of reversible conformational transitions in a single molecule”, 2004, Phys. Rev. Lett. **93**, 196806-196809.

[13] Guisinger, N. P., Greene, M. E., Basu, R., Baluch, A. S., Hersam, M. C.: “Room temperature negative differential resistance through individual organic molecules on silicon surfaces”, 2004, Nano Lett. **4**, 55-59.

[14] Venkataraman, L., Klare, J. E., Tam, I. W., Nuckolls, C., Hybertsen, M. S., Steigerwald, M. L.: “Single-molecule circuits with well-defined molecular conductance”, 2006, Nano Lett. **6**, 458-462.

[15] Atodiresei, N., Brede, J., Lazić, P., Caciuc, V., Hoffmann, G., Wiesendanger, R., Blügel, S.: “Design of the local spin polarization at the organic-ferromagnetic interface”, 2010, Phys. Rev. Lett. **105**, 066601-066604.

[16] Bogani, L., Wernsdorfer, W.: “Molecular spintronics using single-molecule magnets”, 2008, Nat. Mater. **7**, 179-186.

[17] Sanvito, S.: “Molecular spintronics”, 2011, Chem. Soc. Rev. **40**, 3336-3355.

[18] Landauer, R.: “Conductance determined by transmission: probes and quantised constriction resistance”, 1989, J. Phys. Condens. Matt. **1**, 8099-8110.

[19] Takayanagi, K.: “*Proceedings of the International Symposium, 7th*”, Hatoyama, Japan, (Ed. by Y. A. Ono, K. Fujikawa, World Scientific Publishing Co., Singapore, 2002), pp. 27-30.

[20] Van Ruitenbeek, J. M.: “*Quantum Mesoscopic Phenomena and Mesoscopic Devices in Microelectronics*”, (Ed. by I. O. Kulik, R. Ellialtolu, 2000), pp. 35-50.

[21] Kouwenhoven, L. P., Marcus, C. M., Mceuen, P. L., Tarucha, S., Westervelt, R. M., Wingreen, N. S.: “Electron transport in quantum dots” in “*Mesoscopic Electron Transport*”, (Ed. by L. L. Sohn, L. P. Kouwenhoven, G. Schön, Plenum, New York

and London, 1997), pp. 105-214.

[22] Park, J.: "Electron transport in single molecule transistors", (PhD Thesis, University of California, Berkeley, 2003).

[23] Tivanski, A. V., Bemis, J. E., Akhremitchev, B. B., Liu, H., Walker, G. C.: "Adhesion forces in conducting probe atomic force microscopy", 2003, Langmuir **19**, 1929-1934.

[24] Fulton, T. A., Dolan, G. J.: "Observation of single-electron charging effects in small tunnel junctions", 1987, Phys. Rev. Lett. **59**, 109-112.

[25] Chae, D. H., Berry, J. F., Jung, S., Cotton, F. A., Murillo, C. A., Yao, Z.: "Vibrational excitations in single trimetal-molecule transistors", 2006, Nano Lett. **6**, 165-168.

[26] Kong, S. J., Yenilmez, E., Tombler, T. W., Kim, W., Dai, H.: "Quantum interference and ballistic transmission in nanotube electron waveguide", 2001, Phys. Rev. Lett. **87**, 106801-106804.

[27] Javey, J. G., Wang, Q., Lundstrom, M., Dai, H. J.: "Ballistic carbon nanotube field-effect transistors", 2003, Nat. **424**, 654-657.

[28] Durrani, Z. A. K., Raq, M. A: "Electronic transport in silicon nanocrystals and nanochains", 2009, Microelectronic Engineering **86**, 456466.

[29] Park, J., Pasupathy, A. N., Goldsmith, J. I. et al.: "Coulomb blockade and the Kondo effect in single-atom transistors", 2002, Nat. **417**, 722-725.

[30] Liang, W., Shores, M. P., Bockrath, M., Long, J. R., Park, H.: "Kondo resonance in a single-molecule transistor", 2002, Nat. **417**, 725-729.

[31] Huang, D. H., Niu, Q., Antoniewicz, P. R.: "Periodic conductance resonance in a constricted channel", J1991, . Phys.: Condens. Matt. **3**, 9989-9994.

[32] Meir Y., Wingreen N. S., Lee, P. A.: "Transport through a strongly interacting electron system: theory of periodic conductance oscillations", 1991, Phys. Rev. Lett. **66**, 3048-3051.

[33] Landauer, R.: "*Localization, Interaction and Transport Phenomena*", (Springer Series in Solid State Sciences, vol. 61, Ed. by B. Kramer, G. Bergmann and Y. Bruynseraede, New York, Springer, 1985), pp. 38-50.

[34] Meirav U., Kastner M. A., Wind, S. J.: "Single-electron charging and periodic conductance resonances in GaAs nanostructures", 1990, Phys. Rev. Lett. **65**, 771-774.

[35] Lyo, S. K. and Huang, D. H.: "Quantized magneto-thermopower in tunnel-coupled ballistic channels: sign reversal and oscillations", 2004, J. Phys.: Condens. Matt. **16**, 3379-3384.

[36] Streda, P.: "Quantised thermopower of a channel in the ballistic regime", 1989, J. Phys.: Condensed Matt, **1**, L1025-L1027.

[37] Huang, D. H., Easter, M., Gumbs, G., Maradudin, A. A., Lin, S.-Y., Cardimona, D. A., Zhang X.: "Controlling quantum-dot light absorption and emission by a surface-plasmon field", 2014, Opt. Expr. **22**, 27576-27605.

[38] Huang, D. H., Alsing, P. M., Apostolova, T., Cardimona, D. A.: "Coupled energy-drift and force-balance equations for high-field hot-carrier transport", 2005, Phys. Rev. B **71**, 195205.

[39] Maradudin, A. A., Mills, D. L.: "Scattering and absorption of electromagnetic radiation by a semi-infinite medium in the presence of surface roughness", 1975, Phys. Rev. B **11**, 1392-1415.

[40] Schmitt-Rink, S., Chemla, D. S., Haug, H.: "Nonequilibrium theory of the optical Stark effect and spectral hole burning in semiconductors", 1988, Phys. Rev. B **37**, 941-955.

[41] Xu, B., Li, X., Xiao, X., Sakaguchi, H. Tao, N.: "Electromechanical and conductance switching properties of single oligothiophene molecules", 2005, Nano Lett. **5**, 1491-1495.

[42] Xiao, X., Xu, B., Tao N.: "Conductance titration of single-peptide molecules", 2004, J. Am. Chem. Soc. **126**, 53705371.

[43] Wang, W., Lee, T., Reed, M. A.: "Elastic and inelastic electron tunnelling in alkane self-assembled monolayers", 2004, J. Phys. Chem. B. **108**, 1839818407.

[44] Kushmerick, J. G., Lazorcik, J., Patterson, C. H., Shashidhar, R., Seferos, D. S., Bazan, G. C.: "Vibronic contributions to charge transport across molecular junctions", 2004, Nano Lett. **4**, 639-642.

[45] Chen, Y. C., Zwolak, M., Di Ventra, M.: "Local heating in nanoscale conductors", 2003, Nano Lett. **3**, 16911694.

[46] Kim, B., Beebe, J. M., Jun, Y., Zhu, X. Y., Frisbie C. D.: "Correlation between HOMO alignment and contact resistance in molecular junctions: aromatic thiols versus aromatic isocyanides", 2006, J. Am. Chem. Soc. **128**, 4970-4971.

[47] Scudiero, L., Barlow, D. E., Mazur, U., Hipps, K. W.: "Scanning tunnelling microscopy, orbital-mediated tunnelling spectroscopy, and UV photoelectron spectroscopy of metal(II) tetraphenylporphyrins deposited from vapour", 2001, J. Am. Chem. Soc. **123**, 4073-4080.

[48] Alessandrini, A., Salerno, M., Frabboni, S., Facci P.: "Single-metalloprotein wet biotransistor", 2005, Appl. Phys. Lett. **86**, 133902.

[49] Hansen, A. G., Wackerbarth, H., Nielsen, J. U., Zhang, J., Kuznetsov, A. M., Ulstrup, J.: "Nanoscale and single-molecule interfacial electron transfer", 2003, Russ. J. Electrochem **39**, 108-117.

[50] Smit, R. H. M., Noat, Y., Untiedt, C., Lang, N. D., Van Hemert, M. C., Ruitenbeek, J. M.: "Measurement of the conductance of a hydrogen molecule", 2002, Nature **419**, 906-909.

[51] Reed, M. A., Zhou, C., Muller, C. J., Burgin, T. P., Tour, J. M.: "Conductance of a molecular junction", 1997, Sci. **278**, 252-254.

[52] Salomon, A., Cahen, D., Lindsay, S., Tomfohr, J., Engelkes, V. B., Frisbie, C. D.: "Comparison of electronic transport measurements on organic molecules", 2003, Adv. Mater. **15**, 18811890.

[53] Tomfohr, J., Ramachandran, G., Sankey, O. F., Lindsay, S. M.: "Making Contacts to Single Molecules: Are We Nearly There Yet ?", in "*Introducing Molecular Electronics*", (Ed. by G. Fagas, K. Richter, Berlin: Springer, 2005).

[54] Ayub, M., Ivanov, A., Hong, J., Kuhn, P., Instuli, E., Edel, J. B., Albrecht, T.: "Precise electrochemical fabrication of sub-20 nm solid-state nanopores for single-molecule biosensing", 2010, J. Phys. Condens. Matt. **22**, 454128.

[55] Son, J. Y., Song, H.: "Molecular scale electronic devices using single molecules and molecular monolayers", 2013, Curr. Appl. Phys. **13**, 1157-1171.

[56] Gimzewski, J. K., Joachim, C.: "Nanoscale science of single molecules using local probes", 1999, Sci. **283**, 1683-1688.

[57] Selzer, Y., Cabassi, M. A., Mayer, T. S., Allara, D. L.: "Thermally activated conduction in molecular junctions", 2004, J. Am. Chem. Soc. **126**, 4052-4053.

[58] Hall, L. E., Reimers, J. R., Hush, N. S., Silverbrook, K.: "Formalism, analytical model, and a priori Greens-function-based calculations of the currentvoltage characteristics of molecular wires", 2000, J. Chem. Phys. **112**, 1510-1521.

[59] Ventra, M. D., Pantelides, S. T., Lang, N. D. : "First-principles calculation of transport properties of a molecular device", 2000, Phys. Rev. Lett. **84**, 979-982.

[60] Ren, Y., Yu, W. W., Frolov, S. M., Folk, J. A., Wegscheider, W.: "Zero-bias anomaly of quantum point contacts in the low-

conductance limit", 2010, Phys. Rev. B **82**, 045313-045317.
[61] Agrait, N., Yeyati, A. L., Van Ruitenbeek, J. M.: "Quantum properties of atomic-sized conductors", 2003, Phys. Rep. **377**, 81-380.
[62] Krans, J. M., Ruitenbeek, J. M., Fisun, V. V., Yanson, I. K., L Jongh,. J. D.: "The signature of conductance quantization in metallic point contacts", 1995, Nat. **375**, 767-769.
[63] Scheer, E., Agraït, N., Cuevas, J. C. et al.: "The signature of chemical valence in the electrical conduction through a single-atom contact", 1998, Nat. **394**, 154-157.
[64] Moresco, F.: "Manipulation of large molecules by low-temperature STM: model systems for molecular electronics", 2004, Phys. Rep. **399**, 175-225.
[65] Cui, X. D., Primak, A., Zarate, X. et al.: "Reproducible measurement of single-molecule conductivity", 2001, Sci. **294**, 571-574.
[66] Herz, M., Giessib, F. J., Mannhart, J.: "Probing the shape of atoms in real space", 2003, Phys. Rev. B **68**, 045301-045307.
[67] Andres, R. P., Bein, T., Dorogi, M.: "Coulomb staircase at room temperature in a self-assembled molecular nanostructure", 1996, Sci. **272**, 1323-1325.
[68] Ramachandran, G. K., Tomfohr, J. K., Li, J. et al.: "Electron transport properties of a carotene molecule in a metal-(single molecule)-metal junction", 2003, J. Phys. Chem. **107**, 6162-6169.
[69] Samanta, M. P., Tian, W., Datta, S., Henderson, J. I., Kubiak, C. P.: "Electronic conduction through organic molecules", 1996, Phys. Rev. B. **53**, R7626-R7629.
[70] Reichert, T. M., Butt, H., Gross, H.: "STM of metal embedded and coated DNA and DNA-protein complexes", 1996, J. Microscopy **182**, 169-176.
[71] Armstrong, F. A.: "Electron transfer and coupled processes in protein film voltammetry", 1999, Biochem. Soc. Trans. **27**, 206-210.
[72] Friis, E. P., Andersen, J. E. T., Kharkats, Y. I. et al.: "An approach to long-range electron transfer mechanisms in metalloproteins: In situ scanning tunneling microscopy with submolecular resolution", 1999, Proc Nat. Acad. Sci. **96**, 1379-1384.
[73] Sumi, H.: "Electron flow through metalloproteins", 2010, Biochimica et Biophysica Acta **1797**, 1563-1572.
[74] Dunlap, D. D., Garca, R., Schabtach, E., Bustamante, C.: "Masking generates contiguous segments of metal-coated and bare DNA for scanning tunneling microscope imaging", 1993, Proc. Natl. Acad. Sci. **90**, 7652-7655.
[75] Fink, H.-W., Schenberger, C.: "Electrical conduction through DNA molecules", 1999, Nat. **398**, 407-410.
[76] Porath, D., Bezryadin, A., de Vries, S., Dekkar, C.: "Direct measurement of electrical transport through DNA molecules", 2000, Nat. **403**, 635-638.
[77] Kasumov, A. Y., Kociak, M., Gueron, S. et al.: "Proximity-induced superconductivity in DNA", 2001, Sci. **291**, 280-282.
[78] Kratochvlov, I., Král, K Bunček,. M. et al.: "Scanning tunnelling spectrosopy study of DNA conductivity", 2008, Cent. Eur. J. Phys. **6**, 422-426.
[79] Taton, T. A., Mirkin, C. A., Letsinger, R. L.: "Scanometric DNA array detection with nanoparticle probes", 2000, Sci. **289**, 1757-1760.
[80] Winfree, E., Liu, F., Wenzler, L. A., Seeman, N. C.: "Design and self-assembly of two-dimensional DNA crystals", 1998, Nat. **394**, 539-544.
[81] Lauritsen, J. V., Besenbacher, F:. "Model catalyst surfaces investigated by scanning tunnelling microscopy", 2006, Adv. Catal. **50**, 97-147.
[82] Wassel, R. A., Credo, G. M., Fuierer, R. R., Feldheim, D. L., Gorman, C. B.: "Attenuating negative differential resistance in an electroactive self-assembled monolayer-based junction", 2004, J. Am. Chem. Soc. **126**, 295-300.
[83] Piva, P. G., DiLabio, G. A., Pitters, J. L. et al.: "Field regulation of single-molecule conductivity by a charged surface atom", 2005, Nat. **435**, 658-661.
[84] Reed, M. A.: "Inelastic electron tunneling spectroscopy", 2008, Mater. Today **11**, 4650.
[85] Xu, B. Q., Xiao, X. Y., Tao, N. J.: "Measurement of single molecule electromechanical properties", 2003, J. Am. Chem. Soc. **125**, 16164-16165.
[86] Xu, B., Li, X., Xiao, X., Sakaguchi, H., Tao, N.: "Electromechanical and conductance switching properties of single oligothiophene molecules", 2005, Nano Lett. **5**, 1491-1495.
[87] Leatherman, G., Durantini, E. N., Gust, D. et al.: "Carotene as a molecular wire: conducting atomic force microscopy", 1999, J. Phys. Chem. B **103**, 4006-4010.
[88] Wold, D. J., Frisbie, C. D.: "Formation of metalmoleculemetal tunnel junctions: microcontacts to Alkanethiol monolayers with a conducting AFM tip", 2000, J. Am. Chem. Soc. **122**, 2970-2971.
[89] Willemsen, O. H., Snel, M. M., Cambi, A., Greve, J., De Grooth, B. G., Figdor, C. G.: "Biomolecular interactions measured by atomic force microscopy", 2000, Biophys J. **79**, 3267-3281.
[90] Pfreundschuh, M., Martin, D. M., Mulvihill, E., Wegmann, S., Muller, D. J.: "Multiparametric high-resolution imaging of native proteins by force-distance curvebased AFM", 2014, Nat. Protocols **9**, 1113-1130.
[91] Hohmura, K. I., Itokazu, Y., Yoshimura, S. H. et al.: "Atomic force microscopy with carbon nanotube probe resolves the subunit organization of protein complexes", 2000, J. Electr. Microsc. **49**, 415-421.
[92] Wooley, A. T., Cheung, C. L., Hafner, J. H., Lieber, C. M.: "Structural biology with carbon nanotube AFM probes", 2000, Chem. Biology **7**, R193-R204.
[93] Woolley, A. T., Guillemette, C., Cheung, C. L., Housman, D. E., Lieber, C. M.: "Direct haplotyping of kilobase-size DNA using carbon nanotube probes", 2000, Nat. Biotechnol. **18** 760-763.
[94] Ouyang, J., Chu, C.-W., Szmanda, C., Ma, L., Yang, Y.: "Programmable polymer thin film and nonvolatile memory device", 2004, Nat. Mater. **3**, 918-922.
[95] Zhou, C., Deshpande, M. R., Reed, M. A., Jones II, L., Tour, J. M.: "Nanoscale metal/self-assembled monolayer/metal heterostructures", 1997, Appl. Phys. Lett. **71**, 611-613.
[96] Dekker, C.: "Solid-state nanopores" 2007, Nat. Nanotech. **2**, 209-215.
[97] Clarke, J., Wu, H. C., Jayasinghe, L., Patel, A., Reid, S., Bayley H.: "Continuous base identification for single-molecule nanopore DNA sequencing", 2009, Nat. Nanotech. **4**, 265-270.
[98] Wanunu, M., Dadosh, T., Ray, V., Jin, J., McReynolds, L., Drndić, M.: "Rapid electronic detection of probe-specific microRNAs using thin nanopore sensors", 2010, Nat. Nanotech. **5**, 807-814.
[99] Wang, Y., Zheng, D., Tan, Q., Wang, M. X., Gu, L. Q.: "Nanopore-based detection of circulating micro-RNAs in lung cancer patients", 2011, Nat. Nanotech. **6**, 668-674.
[100] Wei, R., Gatterdam, V., Wieneke, R., Tamp, R., Rant, U.: "Stochastic sensing of proteins with receptor-modified solid-state nanopores", 2012, Nat. Nanotech. **7**, 257-263.
[101] Xie, P., Xiong, Q., Fang, Y., Qing, Q., Lieber, C. M.: "Lo-

cal electrical potential detection of DNA by nanowirenanopore sensors", 2012, Nat. Nanotech. **7**, 119-125.

[102] Chen, J., Reed, M. A., Rawlett, A. M., Tour, J. M.: "Large on-off ratios and negative differential resistance in a molecular electronic device", 1999, Sci. **286**, 1550-1552.

[103] Slowinski, K., Fong, H. K. Y., Majda, M.: "Mercury-mercury tunneling junctions: 1. Electron tunneling across symmetric and asymmetric Alkanethiolate bilayers", 1999, J. Am. Chem. Soc. **121**, 7257-7261.

[104] Rampi, M. A., Schueller, O. J. A., Whitesides, G. M.: "Alkanethiol self-assembled monolayers as the dielectric of capacitors with nanoscale thickness", 1998, Appl. Phys. Lett. **72**, 1781-1783.

[105] Selzer, Y., Salomon, A., Cahen, D.: "Effect of molecule-metal electronic coupling on through-bond hole tunneling across metal-organic monolayer-semiconductor junctions", 2002, J. Am. Chem. Soc. **124**, 2886-2887.